Journal of Applied Physics

RESEARCH ARTICLE | NOVEMBER 03 2023

Regulating ferroelectricity in $Hf_{0.5}Zr_{0.5}O_2$ thin films: Exploring the combined impact of oxygen vacancy and electrode stresses

Mingkai Bai ; Peizhen Hong ; Runhao Han ; Junshuai Chai ; Bao Zhang ; Jingwen Hou ; Wenjuan Xiong; Shuai Yang; Jianfeng Gao; Feng Luo ; Zongliang Huo

J. Appl. Phys. 134, 174102 (2023)
https://doi.org/10.1063/5.0170657

Journal of Applied Physics ARTICLE pubs.aip.org/aip/jap

Regulating ferroelectricity in $Hf_{0.5}Zr_{0.5}O_2$ thin films: Exploring the combined impact of oxygen vacancy and electrode stresses

Cite as: J. Appl. Phys. **134**, 174102 (2023); doi: 10.1063/5.0170657
Submitted: 3 August 2023 · Accepted: 23 September 2023 ·
Published Online: 3 November 2023

Mingkai Bai,[1,2] Peizhen Hong,[3,a)] Runhao Han,[1,2] Junshuai Chai,[1,2] Bao Zhang,[1] Jingwen Hou,[1] Wenjuan Xiong,[1] Shuai Yang,[1] Jianfeng Gao,[1] Feng Luo,[3] and Zongliang Huo[1,2,4]

AFFILIATIONS

[1]Institute of Microelectronics, Chinese Academy of Sciences, Beijing 100029, China
[2]College of Microelectronics, University of Chinese Academy of Sciences, Beijing 100049, China
[3]College of Electronic Information and Optical Engineering, Nankai University, Tianjin 300071, China
[4]Yangtze Memory Technologies Company Ltd., Wuhan, China

[a)]**Author to whom correspondence should be addressed:** hongpeizhen@nankai.edu.cn

ABSTRACT

$Hf_{0.5}Zr_{0.5}O_2$ (HZO) is a promising candidate for low-power non-volatile memory due to its nanoscale ferroelectricity and compatibility with silicon-based technologies. Stress and oxygen vacancy (V_O) are key factors that impact the ferroelectricity of HZO. However, their combined effects have not been extensively studied. In this study, we investigated the impact of the V_O content on HZO thin films' ferroelectricity under different electrode stresses by using TiN and tungsten (W) top electrodes and controlling ozone dose time during HZO deposition. The HZO thin films with W top electrodes exhibit elevated stress levels and a greater abundance of orthorhombic/tetragonal phases, and the HZO thin films with TiN top electrode shows an increase in the monoclinic phase with increasing ozone dose time. The residual polarization (P_r) of the capacitors with TiN and W top electrodes displayed different or even opposing trends with increasing ozone dose time, and the V_O content decreases with increasing ozone dose time for both sets of capacitor samples. We propose a model to explain these observations, considering the combined influence of electrode stresses and V_O on the free and formation energy of the crystalline phase. Increasing the V_O content promotes the transformation of the tetragonal phase to the orthorhombic phase in HZO films with TiN top electrodes, and with W top electrodes, a higher V_O content prevents the tetragonal phase from transforming into the orthorhombic/monoclinic phase. Additionally, an alternative explanation is proposed solely from the perspective of stress. These findings provide valuable insights into the regulation of ferroelectricity in HZO thin films.

I. INTRODUCTION

The ferroelectricity of the silicon-doped HfO_2 thin film was first reported in 2011,[1] and unlike traditional ferroelectric materials such as $SrBi_2Ta_2O_9$ and $Pb(Zr, Ti)O_3$, HfO_2 is compatible with CMOS processes and can be 3D-integrated via well-established atomic layer deposition (ALD) technique.[2,3] In addition, the solid solution $Hf_{0.5}Zr_{0.5}O_2$ (HZO) can exhibit ferroelectricity at lower annealing temperatures (400–600 °C).[4] These advantages have sparked significant interest among researchers who are exploring various applications, including energy harvesters,[5] infrared sensing,[6] nonlinear optics,[7] and memory.[8] Especially in memory applications, its non-volatility, fast access speed, and high storage density have received more attention.[9–11] The ferroelectricity of HZO thin films is attributed to the presence of a non-centrosymmetric orthorhombic phase (o-phase, space group: $Pca2_1$).[12] However, under typical semiconductor processes, HfO_2 thin films do not exhibit ferroelectricity and are mostly found in a polycrystalline form dominated by the monoclinic phase (m-phase, space group: $P2_1/c$) or in an amorphous state.[13,14] To investigate the experimental conditions and underlying mechanisms responsible for stabilizing the ferroelectric o-phase, researchers have conducted extensive experimental and theoretical computational

studies.[15–20] These studies have revealed that several factors influence the ferroelectricity of HZO thin films, including at least annealing temperature,[17] thin film thickness,[21] stress,[22–24] and the presence of oxygen vacancy (V_O).[25,26] Among these factors, stress and V_O have received significant attention and have been widely explored.

In the first reports of ferroelectricity in silicon-doped HfO_2 films, the authors primarily attributed the ferroelectricity to the effect of top electrode stress, known as the "capping effect."[1] Subsequent studies have further indicated that the presence of mechanical stresses is associated with a larger polarization response in HZO thin films and has also been linked to its ferroelectric phase stability.[27] Enhanced ferroelectricity has been observed in HZO thin films when using top and bottom electrodes with lower coefficients of thermal expansion.[22] Moreover, thicker electrodes and substrates with lower coefficients of thermal expansion have also been found to promote greater P_r in HZO thin films, accompanied by the presence of increased in-plane tensile stresses.[23,24,28] These investigations attribute the heightened tensile stresses to the thermal mismatch between the electrode, film, or substrate. The elevated tensile stress levels, in turn, facilitate the transition from the non-ferroelectric tetragonal phase (t-phase, space group: $P4_2/nmc$) to the ferroelectric o-phase during rapid thermal annealing. Recently, Fields *et al.*[29] have discovered that smaller biaxial tensile stresses coincided with the generation of the m-phase through stress evolution measurements at each process step and *in situ* stress measurements during annealing. The stresses applied by the electrodes accounted for only a fraction of the overall stress in the HZO thin film. Additionally, a competitive relationship between biaxial tensile stresses and the formation of the m-phase was observed. Larger tensile stresses in the films were attributed to stress accumulation resulting from the o-/t-phase's inability to transition to the higher molar-volume m-phase. While some findings on stress may appear contradictory,[28,29] it is apparent that the electrodes and substrates with different coefficients of thermal expansion significantly influence the ferroelectricity and stress characteristics of the HZO thin film.[22,23,27,30]

V_O also plays a crucial role in the ferroelectricity of HfO_2-based films, and it can be modulated by controlling the oxidant dose and using different oxidants (e.g., water, ozone, and oxygen) during film deposition.[31–34] Mittmann *et al.*[35] and Pal *et al.*[36] found that V_O significantly impacts the ferroelectricity of HZO thin films, and a certain V_O content is necessary to stabilize the ferroelectricity of HZO thin films. The V_O content strongly influences the stabilization of the ferroelectric o-phase, and even without doping and a top electrode, a sufficiently high content of V_O can stabilize the ferroelectric phase in pure HfO_2 films.[37] Furthermore, theoretical calculations have shown that more V_O decrease the free energy of the ferroelectric o-phase.[26,33,38]

In practical scenarios, however, both the V_O content and the stress in the HZO thin film are affected by the electrodes. For example, a nitride electrode (TiN: thermal expansion coefficient = 9.4×10^{-6}/K) draws oxygen atoms from the film, altering the V_O content,[39] whereas a more stable W electrode (thermal expansion coefficient = 4.5×10^{-6}/K) mitigates the extraction of oxygen atoms from the film.[22,40] Conversely, a RuO_2 electrode (thermal expansion coefficient = 6.4×10^{-6}/K) supplies oxygen atoms to the film, thus reducing the V_O content.[41] As a result, the V_O content in the film may vary when investigating the effects of different electrode stresses, making it challenging to obtain highly reliable results. Currently, there is no definitive study available on the impact of V_O content on the ferroelectricity of HZO thin films under various stress conditions.

In this study, we explored the impact of the V_O content on the ferroelectricity of HZO thin films under different W and TiN electrode stresses. The stress in the films, crystalline phase composition, V_O content, and ferroelectricity were analyzed through stress measurements, grazing incidence x-ray diffraction (GIXRD), x-ray photoelectron spectroscopy (XPS) characterization, and electrical tests, respectively. The films exhibit stronger ferroelectricity and experience higher stress when subjected to the lower thermal expansion coefficient of the W electrode after annealing. Additionally, the V_O content decreases with increasing ozone dose time, and its effect on the ferroelectricity of the HZO thin films depends on the stress magnitude provided by the top electrodes.

II. EXPERIMENTAL

Metal–ferroelectric–metal (MFM) capacitors based on 10 nm-thick HZO films were fabricated, as shown in Fig. 1. Initially, a 100 nm-thick TiN metal layer was deposited as the bottom electrode on a 750 μm p-type wafer. The TiN top electrode was sputter-deposited using a Ti target in an Ar and N_2 environment at 200 °C, and the deposition process was carried out at a pressure of 5 mTorr under a 100 W DC power supply. The growth of 10 nm-thick HZO occurred in an ALD reactor at 300 °C, utilizing TEMA (tetrakis ethylmethylamido)-Hf [$Hf(N(CH_3)(C_2H_5))_4$] and TEMA-Zr [$Zr(N(C_2H_5)CH_3)_4$] as organic precursors for Hf and Zr, respectively, with ozone as the oxygen precursor. A Hf:Zr ratio of 1:1 was achieved by alternating cycles of TEMAHf and TEMAZr precursors. During the deposition process, the ozone dose times were set to 1, 5, and 10 s, while the Hf and Zr precursor

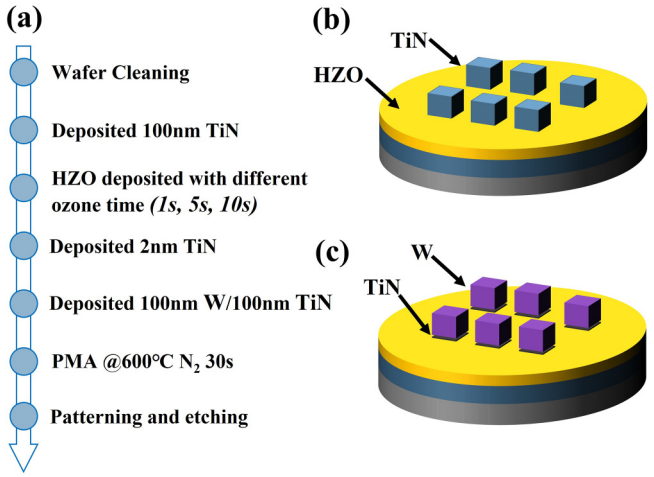

FIG. 1. (a) Process flow of MFM capacitor stacks. (b) The schematic of the MFM capacitor with TiN/HZO/TiN structures and (c) TiN/HZO/TiN/W structures.

dose times and temperatures were kept constant. To ensure the consistency of the electrode interface, all samples were sputtered with a 2 nm layer of TiN by a sputtering process before the deposition of the top electrode. Then, TiN and W of 100 nm were sputtered separately as the top electrode. The TiN deposition conditions were the same as for the bottom electrode. The deposition of the W top electrode was sputtered at room temperature using W targets in an Ar environment, with a working pressure of 10 mTorr and a 5 W DC power supply. The samples were then annealed at 600 °C for 30 s in an N_2 atmosphere to crystallize the HZO films. After post-metallization annealing (PMA), we patterned the samples using photolithography and dry plasma etching to form MFM capacitor structures measuring $70 \times 70\,\mu m^2$.

Electrical characterization was performed using the aixACCT Systems TF Analyzer 3000 instrument (aixACCT Systems GmbH, Aachen, Germany). The analysis included a polarization–electric field hysteresis loop (P–E), and positive-up and negative-down (PUND) pulsed polarization measurements. For the P–E measurement, a triangular pulse with a 3 V amplitude and a 10 kHz frequency was utilized. The PUND measurement employed a trapezoidal pulse with a 3 V amplitude, 10 μs rise and fall times, and 10 μs hold time for both positive and negative pulses. The time interval of each trapezoidal pulse is 1 s.

The radius of curvature of the wafer was measured before and after each process step using a Toho FLX 2320-S to assess changes in film stress. GIXRD measurements were conducted in a parallel beam geometry with a Rigaku SmartLab diffractometer utilizing Cu Kα radiation and incident angle fixed at 0.5°. For further analysis of the crystalline phases, GIXRD data from all samples were imported into Origin software for peak splitting and fitting. Gaussian-fitting was applied to peaks within the 2θ range of 26°–33° to determine the proportions of different phases. XPS measurements using a Thermo Fisher ESCALAB 250Xi device were used to evaluate the content of V_O in the HZO thin films. The XPS measurements were conducted using a monochromatic Al Kα source (1486.7 eV), and the pass energy of 30 eV gave an overall energy resolution of 0.05 eV. Deconvolution of the core level spectra was performed using the Thermo Avantage software, with Shirley type backgrounds. The peaks were modeled with a Voigt function, a convolution of Lorentzian (20%) and Gaussian (80%) functions, and fitting was performed by fixing the separation between each chemical state.

III. RESULTS AND DISCUSSION

To characterize stress changes and verify the hypothesis that different electrodes induce varying stresses, we measured the film's radius of curvature before and after each process step, as illustrated in Fig. 2. We utilized Stoney's equation to calculate the change in biaxial stress values, with Stoney's equation shown as[30,42]

$$\sigma_{\parallel} \times h_f = \frac{E_s t_s^2}{6(1-\upsilon_s)}\left(\frac{1}{R_2} - \frac{1}{R_1}\right), \tag{1}$$

where $\sigma_{||}$, E_s, υ_s, and t_s are the biaxial stress resultant from the process step, elastic modulus (130 GPa), Poisson's ratio (0.28), and thickness of the silicon wafer, respectively; h_f is the thickness of the film; and R_1 and R_2 denote the radius of curvature before and after each process, respectively. The physical meaning of the stress–thickness product value is equal to the membrane force in the film.

The stress–thickness product changes ($\Delta(\sigma_{\parallel} \times h_f)$) for each device before and after each processing step are presented in Figs. 3(a) and 3(b).Following the sputtering of 100 nm-thick TiN bottom electrodes, all devices exhibited a stress–thickness product of approximately -190 ± 10 Pa × m, indicating strong compressive stresses. Subsequent HZO deposition at various ozone dose times showed a minimal variation in the stress–thickness product. Notably, there was a significant stress difference during the deposition of W and TiN top electrodes. The TiN top electrode induced a stress–thickness product change of -140 ± 10 Pa × m, while the W top electrode resulted in a considerably lower change of approximately -20 ± 2 Pa × m. The reasons for the significant stress difference between deposited TiN and W electrodes are described in detail in Sec. 1 in the supplementary material. Due to incomplete crystallization during the deposition of the top electrode (Fig. S1 in the supplementary material), the effect of stress on the crystalline phase may not be significant. After the rapid thermal annealing step, all samples exhibited strong tensile stresses. The samples with W top electrodes displayed even stronger tensile stresses (81 ± 2 to 90 ± 2 Pa × m) compared to those with TiN electrodes (42 ± 2 to 58 ± 2 Pa × m), aligning with findings from previous studies.[22,30,43] Additionally, as shown in Fig. 3(c), the tensile stress for both sets of samples tended to decrease with increasing ozone dose time (5 ± 1.5 Pa × m).

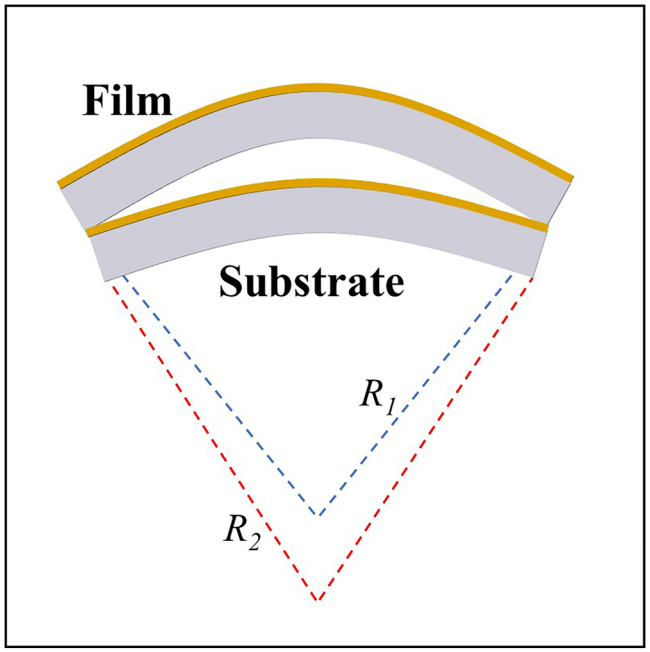

FIG. 2. Schematic diagram showing the measurement of the wafer curvature before and after each process step. R_1 and R_2 represent the radii of curvature of the wafer.

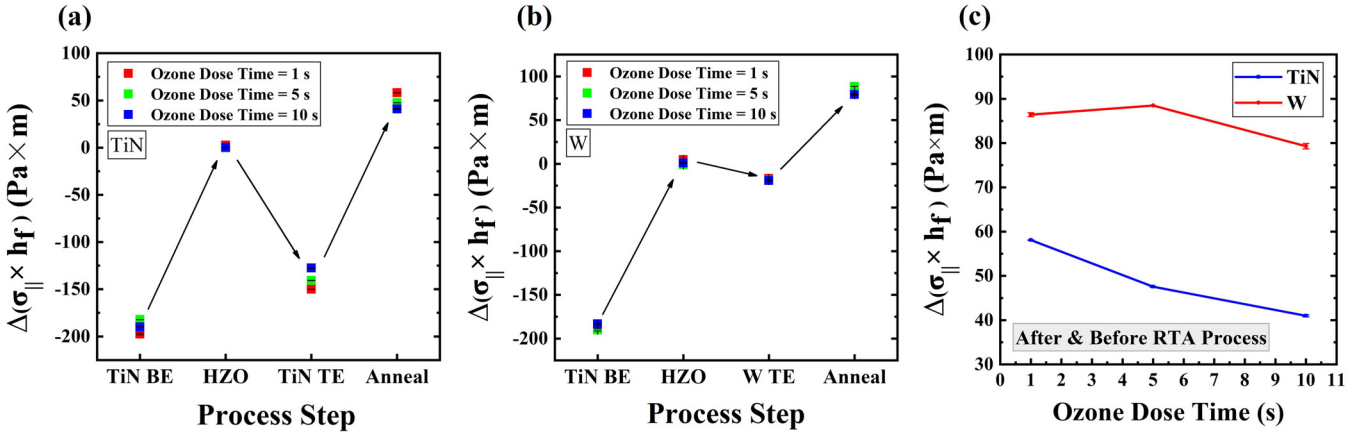

FIG. 3. (a) and (b) Stress–thickness product variation values before and after each process step for TiN and W top electrodes at various ozone dose times. (c) Stress–thickness product variation as a function of ozone dose time after and before rapid thermal annealing.

Considering the thinness of HZO thin films (~10 nm) and their deposition on substrates with thicknesses of hundreds of micrometers away from the mechanical neutral axis,[44,45] the effect of the top electrode on stress alone may not sufficiently explain the observed change in stress values. Moreover, it is important to acknowledge that the stress value obtained through Stoney's equation represents the integrated stress of the entire film, and direct derivation of stress within the HZO layer is not feasible.[29] However, by assuming an ideal film with uniform properties and undergoing only elastic deformation, we can separate the stress–thickness product obtained from Stoney's equation into contributions from different layers,[27,29]

$$\sigma_{\parallel} \times h_f = \sigma_{BE} h_{BE} + \sigma_{HZO} h_{HZO} + \sigma_{TE} h_{TE}, \quad (2)$$

where σ_i and h_i are the ith layer stress and thickness, respectively. BE and TE are the bottom electrode and top electrode, respectively. Directly deriving stresses in individual films without knowing their proportional distribution is not feasible. Assuming that stresses are distributed according to the inverse ratio of the thicknesses, the stress–thickness in HZO can reach up to about 73.8 Pa m (7.38 GPa), and the stress–thickness product change after annealing of the whole film is at most about 91 Pa × m. This significant stress cannot be solely attributed to the thermal mismatch of the electrodes.[27,44] We learned that the final stress in a thin film is related to a variety of factors,[27,29] and stress contributions in each film layer can be subdivided into (i) internal stresses from the deposition process, (ii) phase transition, and (iii) thermal expansion mismatch.[29] The stress results show a minimal change during HZO deposition but a substantial change during top electrode deposition. Considering the films' lack of crystallization at this stage, it is likely that the stress changes during the crystallization process result from a combination of thermal mismatch and phase transition.

GIXRD measurements analyzed the crystal structure and crystalline phase composition of HZO thin films, investigating the impact of stress and oxidant dose on phase formation. As illustrated in Figs. 4(a) and 4(b), the peak 2θ = 30.3° is often a combination of o-phase and t-phase peaks due to their structural similarity [o(111) and t(011)], making peak differentiation challenging.[30] Both sample sets displayed a prominent peak at this position, indicating a higher presence of o-/t-phases. In samples with a TiN top electrode, the intensity of the o-/t-phase peak decreased with increasing ozone dose time, while the intensity of the m(-111) peak increased. Conversely, for samples with a W top electrode, no m-phase related peaks were observed, and the intensity of the o-/t- phase peaks remained nearly constant with increasing ozone dose time. To further analyze the relative content of the crystalline phases, we conducted a split-peak fit to the data in the 26°–33° range. Previous studies have reported o(111) and t(011) peak positions in HZO at approximately 30.3°–30.4° and 30.7°–30.8°, respectively.[39,46,47] Based on Vegard's law,[48] we used a Gaussian function to deconvolute the diffraction peaks of each phase, assigning 2θ values of 28.5°, 30.3°, 30.7°, and 31.8° to m(−111), o(111), t(011), and m(111), respectively. As shown in Figs. 5(a) and 5(b), we ensured data rationality and comparability by setting the full width at half maximum (FWHM) of all crystalline phases to 1° during fitting. The peak splitting results in Fig. 5(c) show that, for the HZO thin film with a TiN top electrode, the o-phase decreases from 65% to ~45% with increasing ozone dose time, the t-phase content also slightly decreases, and the m-phase content increases from 10% to ~35%. Conversely, with a W top electrode, the o-phase content decreases and then increases slightly, while the t-phase content slightly increases and then decreases with increasing ozone dose time. It is important to emphasize that these crystalline phase ratios are relative and composition-dependent, and they do not represent the total crystalline phase ratios within the film since the full spectrum peak map was not considered.

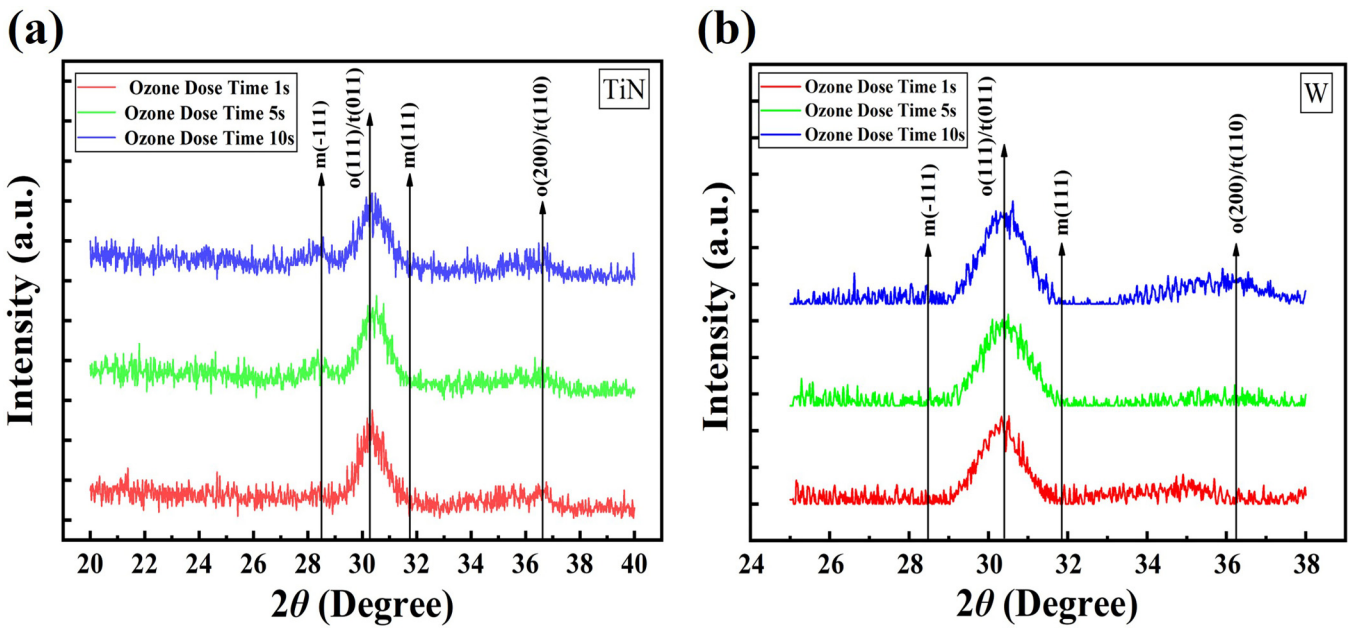

FIG. 4. (a) and (b) The GIXRD pattern of a 10 nm-thick HZO film with TiN and W as the top electrodes after rapid thermal annealing.

Figures 6(a) and 6(b) present typical pristine P–E characteristic curves for samples with TiN and W top electrodes at various ozone dose times. The hysteresis curve for the TiN top electrode capacitance decreases with increasing ozone dose time, while the pattern for the W electrode capacitance appears less clear. To ensure statistical reliability, we conducted ten measurements at different locations on the wafer and obtained the mean and variance of the $2P_r$, as depicted in Fig. 6(c). In the case of the TiN top electrode samples, $2P_r$ decreased from 23 (ozone dose time = 1 s) to 16.5 $\mu C/cm^2$ (ozone dose time = 10 s), consistent with previously reported studies.[26,34,35,49] For the samples using the W electrode, the pristine $2P_r$ initially showed a slight decrease and then increased with ozone dose time, showing a distinct variation compared to the TiN top electrode samples. However, it has also been reported that $2P_r$ increased with ozone dose time when using W electrodes.[40,47] To account for potential leakage variations, we conducted another PUND measurement. The P–E curves of the removed leakage current, shown in Figs. 6(d) and 6(e), mirrored

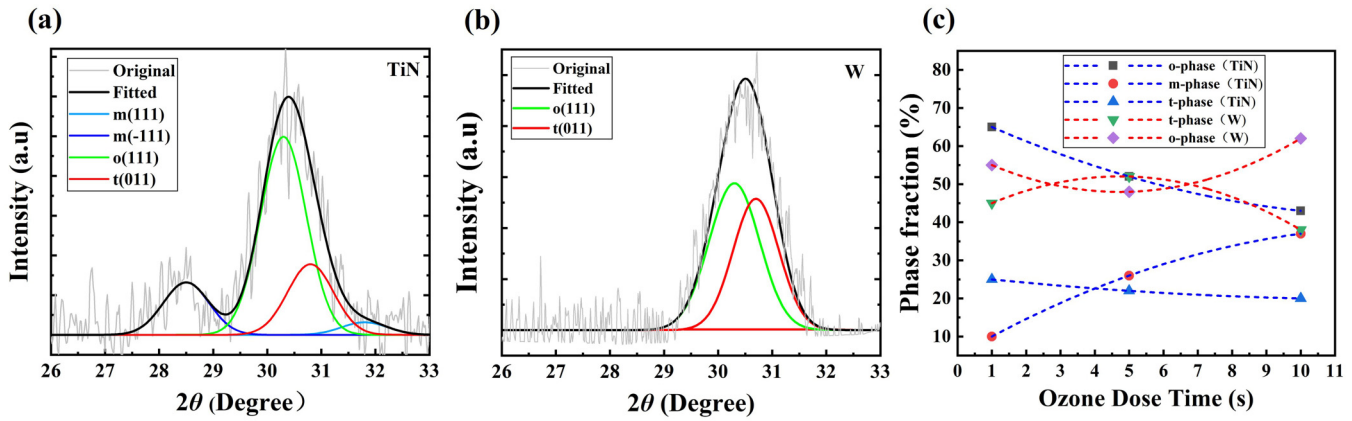

FIG. 5. (a) and (b) Schematic diagrams illustrating the division of peaks for the crystalline phase fitting of HZO films with TiN and W top electrodes. (c) Crystalline phase variation in HZO films with TiN and W top electrodes as a function of ozone dose time.

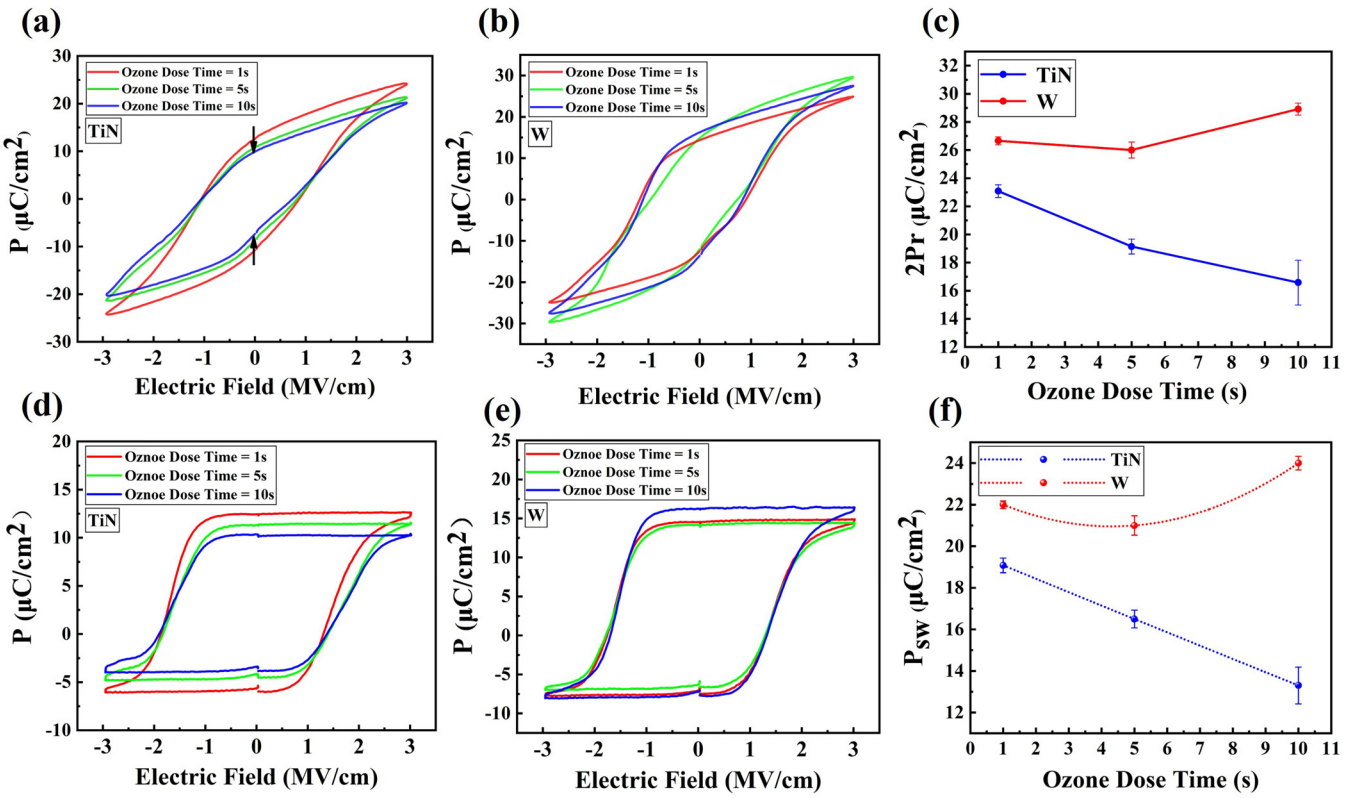

FIG. 6. (a) and (b) Evolution of pristine P–E characteristic curves for samples with TiN and W top electrodes as a function of ozone dose time. (c) Changes in $2P_r$ of HZO films as a function of ozone dose time. (d) and (e) P–E characteristic curves of samples with TiN and W top electrodes after leakage removal, measured by PUND. (f) P_{sw} values plotted against ozone dose time, as measured by PUND.

the same trend as the pristine P–E curves. The amount of polarization switching (P_{sw}) exhibited the same trend as the $2P_r$, as depicted in Fig. 6(f). Comparing the $2P_r$ and P_{sw} values with the relative content of the o-phase, we observed a correlation where larger $2P_r$ values corresponded to a higher relative proportion of the o-phase. The difference between the relative content of the o-phase and the $2P_r$ in the two sets of top electrode samples is explored in Sec. 3 in the supplementary material.

We employed XPS to investigate the effect of different ozone doses on the V_O content within the HZO thin film. XPS is a powerful technique for probing V_O and characterizing thin film oxygen scavenging.[25,50–52] As shown in Figs. 7(a)–7(c) and 7(e)–7(g), the high-resolution spectra of O 1s revealed two distinct peaks at ~529.5 and 531.5 eV for all samples with a takeoff angle of 90° incidence. Previous studies on transition metal oxides associated these peaks with lattice oxygen and vacancy oxygen.[53–55] However, directly using the relative intensity of the peak at ~531.5 eV to determine the V_O content led to an unrealistic value of ~25%. This discrepancy may be due to the presence of C and N in the hafnium and zirconium precursors during the growth process, forming a compound peak with O.[56] Moreover, the peak of adsorbed oxygen (hydroxyl) also appears near 531.5 eV.[57] To obtain qualitative insights into the trend of the V_O content, we compared the normalized O 1s peaks of the two samples.[18,34] In Figs. 7(d) and 7(h), the lattice oxygen signal at 529.5 eV decreases in the intensity as the ozone dose time decreases for the TiN top electrode sample. This decrease is coupled with a shift to higher binding energy. Similarly, for the W top electrode sample, the lattice oxygen signal also decreases in intensity with increasing ozone dose time, accompanied by a shift to higher binding energy values. It indicates an increase in the V_O content for samples with two sets of electrodes.

In addition to utilizing O 1s for analyzing V_O, studying the high-resolution spectra of Hf 4f provides another effective method to assess the V_O content.[18,25] In Fig. 8(a), we present the high-resolution spectra of Hf 4f, controlling the takeoff angle of the HZO film surface at 35°, and calculate the detection depth (d) using the following formula:

$$d = 3\lambda \sin\theta, \tag{3}$$

where λ is the inelastic mean free path of Hf 4f electrons with a value of 2.5 nm and θ is the takeoff angle.[51,58] Based on these calculations, the detection depth was estimated to be 4.3 nm, and the V_O content at this depth was used as the average V_O content within

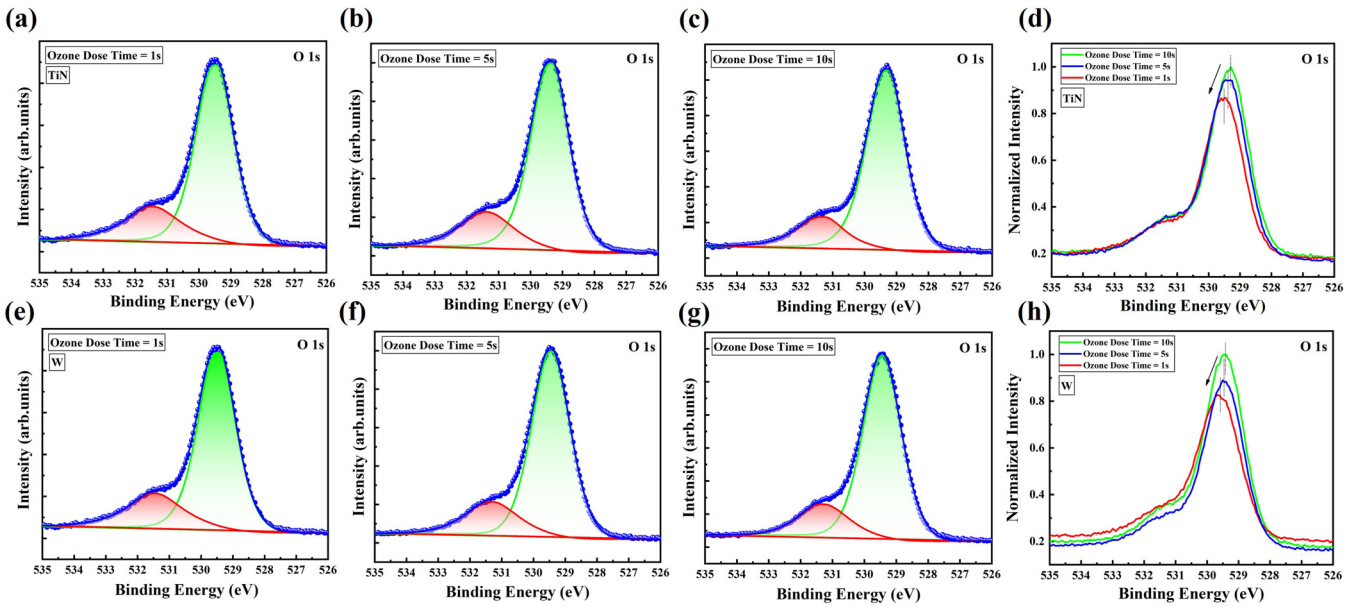

FIG. 7. (a)–(c) and (e)–(g) High-resolution O 1s spectrograms showing HZO films under TiN and W top electrodes at various ozone dose times. (d) and (h) Normalized high-resolution O 1s spectra of TiN and W top electrode samples at different ozone dose times.

the film. The FWHM for Hf 4f was fixed at 1.21 eV, with the spin–orbit splitting set at 1.7 eV, and the branching ratio was 0.75. This approach allowed us to obtain accurate information about the 4f7/2 binding energy and the relative intensity of the Hf^{4+} and Hf^{3+} emissions,[25] with a fixed shift of the binding energy between Hf^{4+} and Hf^{3+} of 1.2 eV. Expectedly, we observed the appearance of additional double peaks located at lower binding energy, which attributed to Hf^{3+} based on a detailed study of the Hf 4f electronic energy spectrum by Suzer *et al.*[52]

Figures 8(b) and 8(d) display the best fits of the Hf 4f spectra, indicating a gradual degradation of Hf^{3+} with increasing ozone dose time. We conducted a quantitative estimation of the V_O content by assuming that each V_O releases two electrons, and considering the HZO stoichiometry, the Hf:O ratio is 1:4, and each V_O releases two Hf^{3+}. The V_O content as a percentage of the total oxygen content was calculated as $1/4 \times 1/2 \times (I^{3+}_{Hf}/I_{total})$, where I^{3+}_{Hf} is the integrated I^{3+}_{Hf} intensity in the core level and I_{total} is the integrated Hf 4f core level intensity. Figure 8(c) illustrates that the V_O content decreased from 0.56% to 0.2% for samples with the TiN electrode and from 0.45% to 0.21% for samples with the W electrode as the ozone dose time increased from 1 to 10 s. Our calculated V_O content matches the published results of Hamouda *et al.*[50,59] The experimental results indicate that the content of V_O decreases with increasing ozone dose time for both samples. It was noted that this method allows us to estimate the content of ionized V_O.[44] However, it should be reasonable as a relative magnitude of the V_O content. In a recent study by Mallick *et al.*,[60] the presence of defect energy levels at 0.6 eV from the HZO conduction band is attributed to V_O, and these levels being near the conduction band edge suggest that V_O is likely to be mostly ionized.

To gain insights into the experimental findings, we conducted further research on the role of the electrode and V_O in stabilizing the ferroelectric o-phase. When using W electrodes with lower coefficients of thermal expansion, we observed an increase in the ferroelectric o-phase along with a greater tensile stress effect. Two capping effect models are proposed to explain the impact of mechanical stresses on the HZO layers.[44] The first model suggests that mechanical confinement during cooling from elevated crystallization temperature prevents the development of mechanical shear strains. The second model proposes that the top electrode imparts stress to the HZO layer, resulting in significant stresses due to differential coefficients of thermal expansion between the electrodes and HZO films. However, both models conflict with thin film mechanics as HZO films are thin (<30 nm) and prepared on substrates located a few hundred micrometers away from the mechanical neutral axis.[45] Referring to Fields *et al.*[44] and considering the effects of differences in the coefficients of thermal expansion of the electrodes. It is plausible that the lower coefficient of thermal expansion of the W electrode promotes the formation of more o-phases during annealing due to a larger thermal mismatch with the HZO film. As a result, the transformation of the t-phase into the larger molar-volume m-phase is hindered, leading to a more pronounced accumulation of stresses. Regarding the HZO films with the TiN top electrode, the smaller thermal mismatch leads to the formation of the m-phase, consequently leading to reduced film stress accumulation.

In samples with W and TiN top electrodes, $2P_r$ and P_{sw} exhibit distinct trends with ozone dose time. Our experiments show that decreasing ozone dose time increases the V_O content, significantly impacting HZO thin film ferroelectricity. Based on the

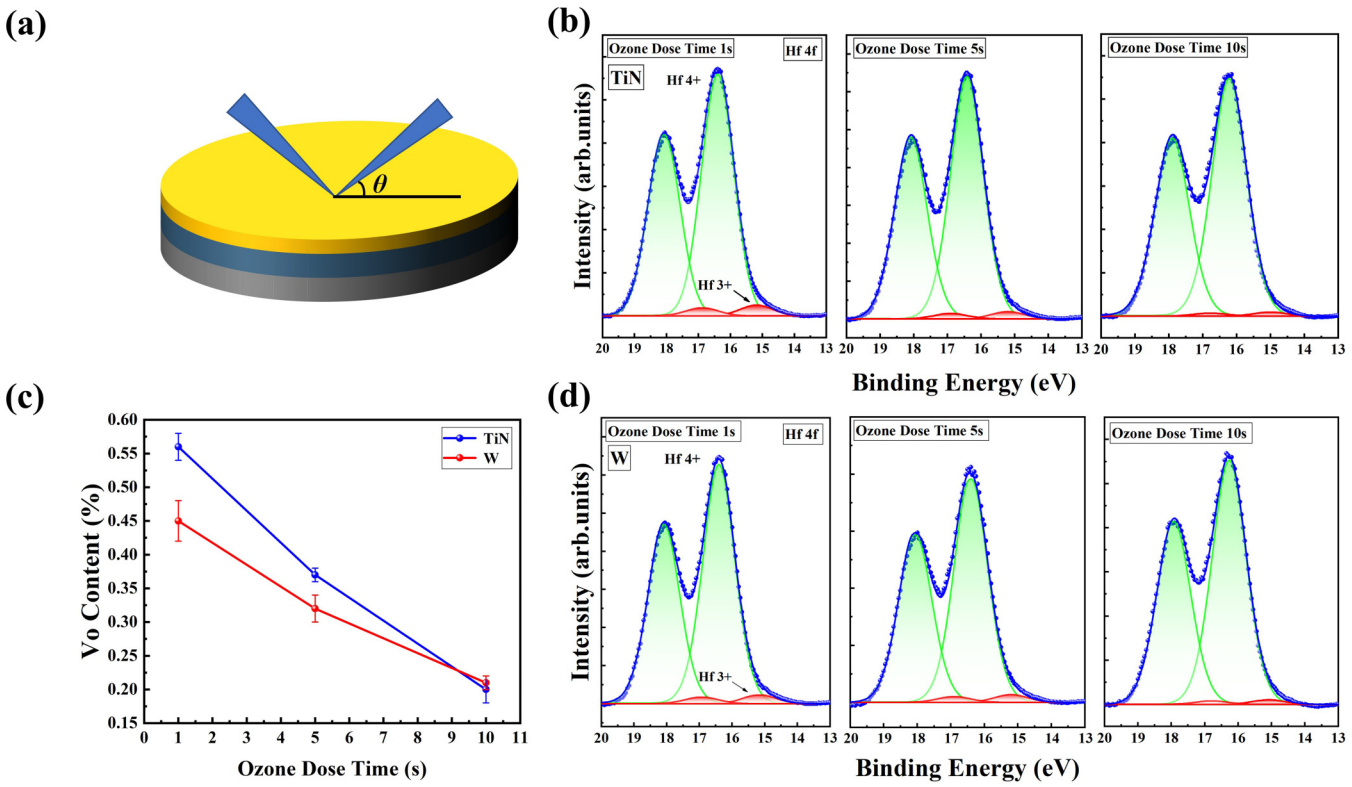

FIG. 8. (a) Schematic diagram of the HZO surface after photolithographic etching of the electrode and detection of V_O by XPS technique. (b) The Hf 4f core level of the HZO sample with the TiN top electrode with a takeoff angle of 35°. (c) V_O content as a function of ozone dose time. (d) The Hf 4f core level of the HZO sample with the W top electrode with a takeoff angle of 35°.

variation in the crystalline phase content with ozone dose time, we propose a physical model that includes the effects of stress and V_O on the thermodynamic free energy of the crystalline phase and the kinetic barrier of the crystalline phase transition.[33,61] This model considers transitions from the t-phase to o-phase and m-phase during crystallization[62,63] and incorporates insights from Liu and Hanrahan[20] and Clima *et al.*,[64] demonstrating that stress and V_O influence transition activation barriers between these phases. As shown in Fig. 9, as the capacitor sample's temperature increases, the HZO thin films undergo a transformation from an amorphous structure to the t-phase. During cooling, if the HZO film experiences lower tensile stress from TiN and has a low V_O content, the o-phase and t-phase exhibit high free energy. The activation barrier for the t-phase to m-phase transition is lower than that for the t-phase to o-phase transition, favoring the formation of the m-phase. Increasing the film's V_O content reduces the free energy of the o-phase and t-phase. It also lowers the activation barrier for the t-phase to o-phase transition, favoring the formation of the o-phase. Previous studies have shown that the activation barrier for the t-phase to o-phase transition (30 meV/f.u.) can be significantly lower than that for the t-phase to m-phase transition (250 meV/f.u.).[65] If the HZO film experiences higher tensile stress from W and has a low V_O content, both the o-phase and t-phase will exhibit high free energy. This heightened stress level results in a lower activation barrier for the t-phase to o-phase transition compared to the t-phase to m-phase transition, favoring the formation of the o-phase. However, when the film's V_O content is increased, the free energies of both the o-phase and t-phase decrease. Simultaneously, the activation barriers for the t-phase to o-phase and t-phase to m-phase transitions increase, hindering the transition to the t-phase. Previous research by Islamov and Perevalov[26] has shown that higher stresses and an increased V_O content lead to the destruction of the ferroelectric o-phase. While the t-phase content does not consistently increase as the ozone dose time decreases in our experiment (e.g., ozone dose time from 5 to 1 s), we suggest that a moderate increase in the V_O content under higher tensile stresses significantly hinders the t-phase transition. Further increases in the V_O content do not seem to notably impact the t-phase. Our study is the first to report that an increase in the V_O content in HZO films under higher stresses promotes the t-phase, providing a plausible explanation for this phenomenon.

The explanation provided above is one of the possible interpretations. Notably, as the V_O content increases, the film stress also rises, as depicted in Fig. 3(c). Previous studies have reported that

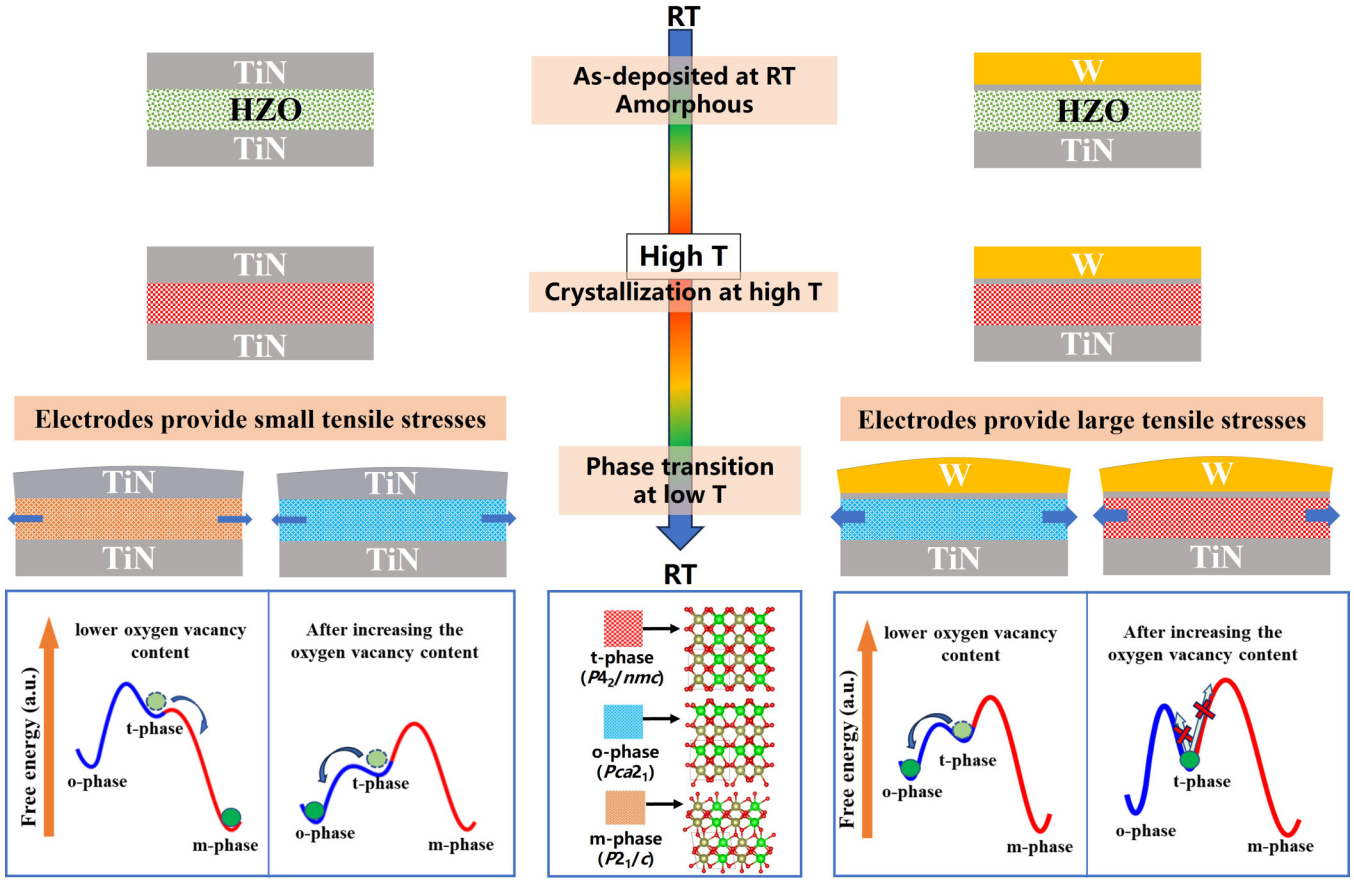

FIG. 9. The schematic diagram of the phase transition process in the rapid thermal annealing of HZO ferroelectric capacitors. The effect of the V_O content on the thermodynamic free energy and kinetic barriers of the crystalline phase in the case of electrodes providing smaller tensile stresses (left, TiN) versus larger tensile stresses (right, W).

reducing the oxygen source dose leads to an increase in wafer tensile stress.[66] This may suggest that the presence of V_O may cause slight lattice deformation, contributing to heightened tensile stress within the film, thereby promoting the stabilization of either the o-phase or t-phase. It is important to emphasize that electrode stress and V_O may interact, rather than acting independently.

IV. CONCLUSIONS

In summary, our study investigated the impact of the V_O content on the ferroelectricity of HZO thin films using TiN and W top electrodes with varying ozone dose times during HZO deposition. We observed that the W top electrode induced greater tensile stresses in the films. Capacitors with TiN and W top electrodes showed opposite trends in P_r with increasing ozone dose time. XPS analysis revealed a decreasing V_O content with higher ozone dose time for capacitors with TiN and W top electrodes. Our findings suggest that the effect of the V_O content has certain prerequisites. For a TiN top electrode, a proper increase in the V_O content leads to the formation of the ferroelectric o-phase, whereas for a W top electrode, a proper increase in the V_O content induces the formation of the t-phase. Additionally, we present a model explaining the variation in the crystalline phase free energy and transformation barrier due to the V_O content at different electrode stresses. Furthermore, another explanation for V_O affecting the stress and, thus, the stability of the crystalline phase is also given. Overall, our findings provide new insights into the effect of V_O on the HZO film ferroelectricity and suggest a novel approach to regulating it.

SUPPLEMENTARY MATERIAL

See the supplementary material for the reason for the significant stress difference after the deposition of the TiN and W top electrodes, the GIXRD data of the unannealed HZO films after the deposition of the top electrodes, and the reason for the difference in the ratio of the o-phase compared to 2Pr for TiN and W top electrode samples.

ACKNOWLEDGMENTS

This project received funding from the Youth Innovation Promotion Association, Chinese Academy of Sciences, under Grant No. 2019117. The authors are grateful to the Integrated Circuit Advanced Process R&D Center (ICAC) of the Institute of Microelectronics of the Chinese Academy (IMECAS) for providing the experimental platform. We thank Tsinghua University for providing the XRD and XPS tests. We thank Professor Xu and Professor Wang (ICAC) for their guidance and suggestions.

AUTHOR DECLARATIONS

Conflict of Interest

The authors have no conflicts to disclose.

Author Contributions

Mingkai Bai: Conceptualization (equal); Data curation (equal); Formal analysis (equal); Investigation (equal); Methodology (equal); Validation (equal); Writing – original draft (equal); Writing – review & editing (equal). **Peizhen Hong:** Conceptualization (equal); Data curation (equal); Funding acquisition (equal); Investigation (equal); Methodology (equal); Resources (equal); Supervision (equal); Writing – original draft (equal); Writing – review & editing (equal). **Runhao Han:** Conceptualization (equal); Data curation (equal); Formal analysis (equal); Investigation (equal); Methodology (equal); Writing – review & editing (equal). **Junshuai Chai:** Conceptualization (equal); Formal analysis (equal); Methodology (equal); Resources (equal); Supervision (equal); Writing – review & editing (equal). **Bao Zhang:** Data curation (equal); Methodology (equal); Resources (equal); Supervision (equal); Writing – review & editing (equal). **Jingwen Hou:** Data curation (equal); Methodology (equal); Resources (equal); Supervision (equal); Writing – review & editing (equal). **Wenjuan Xiong:** Data curation (equal); Methodology (equal); Resources (supporting); Supervision (supporting). **Shuai Yang:** Data curation (equal); Funding acquisition (equal); Methodology (equal); Resources (equal); Supervision (supporting). **Jianfeng Gao:** Data curation (equal); Formal analysis (equal); Methodology (supporting); Resources (equal); Supervision (supporting). **Feng Luo:** Data curation (equal); Funding acquisition (supporting); Methodology (equal); Resources (equal); Supervision (equal); Writing – original draft (equal); Writing – review & editing (equal). **Zongliang Huo:** Data curation (equal); Formal analysis (equal); Funding acquisition (equal); Methodology (equal); Resources (equal); Supervision (equal); Writing – original draft (equal); Writing – review & editing (equal).

DATA AVAILABILITY

The data that support the findings of this study are available from the corresponding author upon reasonable request.

REFERENCES

[1]T. S. Böscke, J. Müller, D. Bräuhaus, U. Schröder, and U. Böttger, Appl. Phys. Lett. **99**, 102903 (2011).
[2]Y.-C. Lien, J.-M. Shieh, W.-H. Huang, W.-S. Hsieh, C.-H. Tu, C. Wang, C.-H. Shen, T.-H. Chou, M.-C. Chen, J. Y. Huang, C.-L. Pan, Y.-C. Lai, C. Hu, and F.-L. Yang, in *International Electron Devices Meeting (IEDM)* (IEEE, 2012), pp. 33.6.1–33.6.4.
[3]N. Gong and T.-P. Ma, IEEE Electron Device Lett. **37**, 1123–1126 (2016).
[4]J. Müller, T. S. Böscke, U. Schröder, S. Mueller, D. Bräuhaus, U. Böttger, L. Frey, and T. Mikolajick, Nano Lett. **12**, 4318–4323 (2012).
[5]M. H. Park, H. J. Kim, Y. J. Kim, T. Moon, K. D. Kim, and C. S. Hwang, Nano Energy **12**, 131–140 (2015).
[6]C. Mart, M. Czernohorsky, S. Zybell, T. Kämpfe, and W. Weinreich, Appl. Phys. Lett. **113**, 122901 (2018).
[7]J. F. Ihlefeld, T. S. Luk, S. W. Smith, S. S. Fields, S. T. Jaszewski, D. M. Hirt, W. T. Riffe, S. Bender, C. Constantin, M. V. Ayyasamy, P. V. Balachandran, P. Lu, M. David Henry, and P. S. Davids, J. Appl. Phys. **128**, 034101 (2020).
[8]J. Müller, T. S. Böscke, S. Muller, E. Yurchuk, P. Polakowski, J. Paul, D. Martin, T. Schenk, K. Khullar, A. Kersch, W. Weinreich, S. Riedel, K. Seidel, A. Kumar, T. M. Arruda, S. V. Kalinin, T. Schlosser, R. Boschke, R. van Bentum, U. Schroder, and T. Mikolajick, in *IEEE International Electron Devices Meeting (IEDM)* (IEEE, 2013), pp. 10.8.1–10.8.4.
[9]S. Mueller, S. R. Summerfelt, J. Müller, U. Schroeder, and T. Mikolajick, IEEE Electron Device Lett. **33**, 1300–1302 (2012).
[10]S. Fujii, Y. Kamimuta, T. Ino, Y. Nakasaki, R. Takaishi, and M. Saitoh, in *IEEE Symposium on VLSI Technology* (IEEE, 2016), pp. 1–2.
[11]F. Ali, T. Ali, D. Lehninger, A. Sünbül, A. Viegas, R. Sachdeva, A. Abbas, M. Czernohorsky, and K. Seidel, Adv. Funct. Mater. **32**, 2201737 (2022).
[12]X. Sang, E. D. Grimley, T. Schenk, U. Schroeder, and J. M. LeBeau, Appl. Phys. Lett. **106**, 162905 (2015).
[13]M. Pešić, F. P. G. Fengler, L. Larcher, A. Padovani, T. Schenk, E. D. Grimley, X. Sang, J. M. LeBeau, S. Slesazeck, U. Schroeder, and T. Mikolajick, Adv. Funct. Mater. **26**, 4601–4612 (2016).
[14]W. Banerjee, A. Kashir, and S. Kamba, Small **18**, e2107575 (2022).
[15]A. G. Chernikova, M. G. Kozodaev, D. V. Negrov, E. V. Korostylev, M. H. Park, U. Schroeder, C. S. Hwang, and A. M. Markeev, ACS Appl. Mater. Interfaces **10**, 2701–2708 (2018).
[16]M. Hyuk Park, H. Joon Kim, Y. Jin Kim, W. Lee, H. Kyeom Kim, and C. Seong Hwang, Appl. Phys. Lett. **102**, 112914 (2013).
[17]S. Park, M. C. Chun, M. J. Kim, J. Y. Lee, Y. Cho, C. Kim, J. Y. Jo, and B. S. Kang, J. Appl. Phys. **129**, 164101 (2021).
[18]L. Baumgarten, T. Szyjka, T. Mittmann, M. Materano, Y. Matveyev, C. Schlueter, T. Mikolajick, U. Schroeder, and M. Müller, Appl. Phys. Lett. **118**, 032903 (2021).
[19]P. Fan, Y. K. Zhang, Q. Yang, J. Jiang, L. M. Jiang, M. Liao, and Y. C. Zhou, J. Phys. Chem. C **123**, 21743–21750 (2019).
[20]S. Liu and B. M. Hanrahan, Phys. Rev. Mater. **3**, 054404 (2019).
[21]M. Hoffmann, U. Schroeder, T. Schenk, T. Shimizu, H. Funakubo, O. Sakata, D. Pohl, M. Drescher, C. Adelmann, R. Materlik, A. Kersch, and T. Mikolajick, J. Appl. Phys. **118**, 072006 (2015).
[22]R. Cao, Y. Wang, S. Zhao, Y. Yang, X. Zhao, W. Wang, X. Zhang, H. Lv, Q. Liu, and M. Liu, IEEE Electron Device Lett. **39**, 1207–1210 (2018).
[23]T. Shiraishi, K. Katayama, T. Yokouchi, T. Shimizu, T. Oikawa, O. Sakata, H. Uchida, Y. Imai, T. Kiguchi, T. J. Konno, and H. Funakubo, Appl. Phys. Lett. **108**, 262904 (2016).
[24]T. Shiraishi, K. Katayama, T. Yokouchi, T. Shimizu, T. Oikawa, O. Sakata, H. Uchida, Y. Imai, T. Kiguchi, T. J. Konno, and H. Funakubo, Mater. Sci. Semicond. Process. **70**, 239–245 (2017).
[25]W. Hamouda, F. Mehmood, T. Mikolajick, U. Schroeder, T. O. Mentes, A. Locatelli, and N. Barrett, Appl. Phys. Lett. **120**, 202902 (2022).
[26]D. R. Islamov and T. V. Perevalov, Microelectron. Eng. **216**, 111041 (2019).
[27]Y. Lee, H. W. Jeong, S. H. Kim, K. Yang, and M. H. Park, Mater. Sci. Semicond. Process. **160**, 107411 (2023).
[28]S. J. Kim, D. Narayan, J.-G. Lee, J. Mohan, J. S. Lee, J. Lee, H. S. Kim, Y.-C. Byun, A. T. Lucero, C. D. Young, S. R. Summerfelt, T. San, L. Colombo, and J. Kim, Appl. Phys. Lett. **111**, 242901 (2017).

[29]S. S. Fields, T. Cai, S. T. Jaszewski, A. Salanova, T. Mimura, H. H. Heinrich, M. D. Henry, K. P. Kelley, B. W. Sheldon, and J. F. Ihlefeld, Adv. Electron. Mater. **8**, 2200601 (2022).
[30]Y. Lee, Y. Goh, J. Hwang, D. Das, and S. Jeon, IEEE Trans. Electron Devices **68**, 523–528 (2021).
[31]A.-J. Cho, J. Jeon, H. K. Chung, I.-H. Baek, K. Yang, M. H. Park, S.-H. Baek, and S. K. Kim, Ceram. Int. **48**, 3280–3286 (2022).
[32]R. Alcala, C. Richter, M. Materano, P. D. Lomenzo, C. Zhou, J. L. Jones, T. Mikolajick, and U. Schroeder, J. Phys. D: Appl. Phys. **54**, 035102 (2021).
[33]Y. Zhou, Y. K. Zhang, Q. Yang, J. Jiang, P. Fan, M. Liao, and Y. C. Zhou, Comput. Mater. Sci. **167**, 143–150 (2019).
[34]T. Mittmann, M. Materano, P. D. Lomenzo, M. H. Park, I. Stolichnov, M. Cavalieri, C. Zhou, C. Chung, J. L. Jones, T. Szyjka, M. Müller, A. Kersch, T. Mikolajick, and U. Schroeder, Adv. Mater. Interfaces **6**, 1900042 (2019).
[35]T. Mittmann, M. Materano, S. C. Chang, I. Karpov, T. Mikolajick, and U. Schroeder, in *IEEE International Electron Devices Meeting (IEDM)* (IEEE, 2020), pp. 18.4.1–18.4.4.
[36]A. Pal, V. K. Narasimhan, S. Weeks, K. Littau, D. Pramanik, and T. Chiang, Appl. Phys. Lett. **110**, 022903 (2017).
[37]S. T. Jaszewski, E. R. Hoglund, A. Costine, M. H. Weber, S. S. Fields, M. G. Sales, J. Vaidya, L. Bellcase, K. Loughlin, A. Salanova, D. A. Dickie, S. L. Wolfley, M. D. Henry, J.-P. Maria, J. L. Jones, N. Shukla, S. J. McDonnell, P. Reinke, P. E. Hopkins, J. M. Howe, and J. F. Ihlefeld, Acta Mater. **239**, 118220 (2022).
[38]T. V. Perevalov, D. R. Islamov, V. A. Gritsenko, and I. P. Prosvirin, Nanotechnology **29**, 194001 (2018).
[39]H. Chen, X. Zhou, L. Tang, Y. Chen, H. Luo, X. Yuan, C. R. Bowen, and D. Zhang, Appl. Phys. Rev. **9**, 011307 (2022).
[40]D. Wang, Y. Zhang, J. Wang, C. Luo, M. Li, W. Shuai, R. Tao, Z. Fan, D. Chen, M. Zeng, J. Y. Dai, X. B. Lu, and J. M. Liu, J. Mater. Sci. Technol. **104**, 1–7 (2022).
[41]Y. Goh, S. H. Cho, S. K. Park, and S. Jeon, Nanoscale **12**, 9024–9031 (2020).
[42]G. G. Stoney, Proc. R. Soc. A **82**, 172–175 (1909).
[43]Y.-K. Liang, J.-W. Lin, Y.-S. Huang, W.-C. Lin, B.-F. Young, Y.-C. Shih, C.-C. Lu, S. H. Yeong, Y.-M. Lin, P.-T. Liu, E. Y. Chang, and C.-H. Lin, ECS J. Solid State Sci. Technol. **11**, 053012 (2022).
[44]J. F. Ihlefeld, S. T. Jaszewski, and S. S. Fields, Appl. Phys. Lett. **121**, 240502 (2022).
[45]L. Freund and S. Suresh, *Thin Film Materials: Stress, Defect Formation, and Surface Evolution* (Cambridge University Press, 2003).
[46]M. Hyuk Park, H. Joon Kim, Y. Jin Kim, T. Moon, and C. Seong Hwang, Appl. Phys. Lett. **104**, 072901 (2014).
[47]H. Kim, A. Kashir, S. Oh, and H. Hwang, Nanotechnology **32**, 055703 (2021).
[48]M. Hyuk Park, H. Joon Kim, Y. Jin Kim, W. Lee, T. Moon, and C. Seong Hwang, Appl. Phys. Lett. **102**, 242905 (2013).
[49]A. Kashir, H. Kim, S. Oh, and H. Hwang, ACS Appl. Electron. Mater. **3**, 629–638 (2021).
[50]W. Hamouda, A. Pancotti, C. Lubin, L. Tortech, C. Richter, T. Mikolajick, U. Schroeder, and N. Barrett, J. Appl. Phys. **127**, 064105 (2020).
[51]M. Su, J. Liu, Z. Weng, X. Ding, Z. Chen, Y. Zhang, L. Zhao, C. Lee, and Y. Zhao, Appl. Phys. Express **14**, 126503 (2021).
[52]S. Suzer, S. Sayan, M. M. Banaszak Holl, E. Garfunkel, Z. Hussain, and N. M. Hamdan, J. Vac. Sci. Technol. A **21**, 106–109 (2003).
[53]S. Peng, F. Gong, L. Li, D. Yu, D. Ji, T. Zhang, Z. Hu, Z. Zhang, S. Chou, Y. Du, and S. Ramakrishna, J. Am. Chem. Soc. **140**, 13644–13653 (2018).
[54]B. Zhang, L. Wang, Y. Zhang, Y. Ding, and Y. Bi, Angew. Chem., Int. Ed. **57**, 2248–2252 (2018).
[55]Z. Wang, X. Mao, P. Chen, M. Xiao, S. A. Monny, S. Wang, M. Konarova, A. Du, and L. Wang, Angew. Chem., Int. Ed. **58**, 1030–1034 (2019).
[56]H. A. Hsain, Y. Lee, P. D. Lomenzo, R. Alcala, B. Xu, T. Mikolajick, U. Schroeder, G. N. Parsons, and J. L. Jones, J. Appl. Phys. **133**, 225304 (2023).
[57]H. Idriss, Surf. Sci. **712**, 121894 (2021).
[58]X. Xu, G. Feng, W. Peng, J. Teng, G. Han, R. Guo, X. Xiong, X. He, J. Luo, C. Feng, and G. Yu, AIP Adv. **10**, 065109 (2020).
[59]F. P. G. Fengler, R. Nigon, P. Muralt, E. D. Grimley, X. Sang, V. Sessi, R. Hentschel, J. M. LeBeau, T. Mikolajick, and U. Schroeder, Adv. Electron. Mater. **4**, 1700547 (2018).
[60]A. Mallick, M. K. Lenox, T. E. Beechem, J. F. Ihlefeld, and N. Shukla, Appl. Phys. Lett. **122**, 132902 (2023).
[61]R. Materlik, C. Künneth, M. Falkowski, T. Mikolajick, and A. Kersch, J. Appl. Phys. **123**, 164101 (2018).
[62]M. H. Park, Y. H. Lee, T. Mikolajick, U. Schroeder, and C. S. Hwang, Adv. Electron. Mater. **5**, 1800522 (2019).
[63]T. D. Huan, V. Sharma, G. A. Rossetti, and R. Ramprasad, Phys. Rev. B **90**, 064111 (2014).
[64]S. Clima, S. R. C. Mcmitchell, K. Florent, L. Nyns, and G. Pourtois, in *International Electron Devices Meeting (IEDM)* (IEEE, 2018), pp. 16.5.1–16.5.4.
[65]M. H. Park, Y. H. Lee, H. J. Kim, Y. J. Kim, T. Moon, K. D. Kim, S. D. Hyun, T. Mikolajick, U. Schroeder, and C. S. Hwang, Nanoscale **10**, 716–725 (2018).
[66]S. Jena, R. B. Tokas, J. S. Misal, K. D. Rao, D. V. Udupa, S. Thakur, and N. K. Sahoo, Thin Solid Films **592**, 135–142 (2015).